6 | Results for deformed nuclei

Having established that the code works as expected for spherical nuclei, we can extend the calculations to deformed systems. In this chapter, the GCG implementation is validated against well established deformed codes and some interesting results regarding α-clustering and drip line nuclei are presented.

This chapter is organised as follows, first in section 6.1, the quadrupole deformation parameter β_2 is presented, and its two different definitions are compared. Then, in section 6.2, results for the super-deformed ^{24}Mg are presented and used as a benchmark for the performance of our code against the HO basis expansion code HFBTHO in section 6.2.1, and then against the cartesian mesh code EV8 in section 6.2.2. Finally, in section 6.3, results about further deformed nuclei are presented, more specifically, in section 6.3.1 results regarding an alpha-clustering study in 20^{20}Ne are shown, and in section 6.3.2 the results for the drip line nuclei ^{42}Si and ^{28}S are presented.

6.1. Deformation parameters

When dealing with deformed nuclei, mean square radii are not sufficient to characterize the nuclear density. The main parameter used is the quadrupole deformation parameter β_2, similar to the one encountered in section 1.3, it can be computed through the mean square radius as

$$\beta_2 = \frac{4\pi \langle \mathcal{Q}_{20} \rangle}{5A \langle r^2 \rangle}, \tag{6.1}$$

where $\langle r^2 \rangle$ is the total mean square radius of the nucleus

$$\langle r^2 \rangle = \frac{\int (\rho_n + \rho_p) r^2 d\boldsymbol{r}}{\int (\rho_n + \rho_p) d\boldsymbol{r}} = \langle x^2 + y^2 + z^2 \rangle. \tag{6.2}$$

Alternatively, it is possible to normalise with respect to the parametetrised nuclear radius in formula (1.6), which yields

$$\beta_2 = \frac{4\pi \langle \mathcal{Q}_{20} \rangle}{3AR^2} \tag{6.3}$$

where the relation

$$\langle r^2 \rangle = \frac{3}{5} R^2 \tag{6.4}$$

is used, and the value for r_0 is taken to be 1.2, in accordance with the one used in other codes [78].

Using either of the two formulae (6.1, 6.3), because of the normalization with respect to the total radius and mass, the β_2 parameter allows the comparison of different nuclei across the chart.

The choice of β_2 used in the following sections depends on the code which is used to benchmark the results. For comparisons with `HFBTHO`, formula (6.1) is used, while for `EV8` comparisons and results in other sections, formula (6.3) is used. In figure 6.1, a comparison between the two formulae is presented; as shown by the shape of the curves, it's possible to observe that the normalisation of β_2 with respect to the real radius has an asymptotic behaviour for large deformations, since for large $\langle z^2 \rangle$, assuming axial symmetry and constant volume V

$$\beta_2 \propto \frac{2z^2 - 2V/z}{z^2 + 2V/z} \xrightarrow[z \to \infty]{} 2, \tag{6.5}$$

while normalising with respect to the parametrised radius R has no such asymptotic behaviour, since R is constant for any deformation.

6.2. ^{24}Mg Benchmarks

In the following section, results for ^{24}Mg are presented and used as a benchmark for the performance of our code in a deformed case. ^{24}Mg is a light, deformed nucleus, whose pairing correlations are negligible in its ground state and for deformations around it.

In section 6.2.1, the axially symmetric HO basis code `HFBTHO` is used, since it is a well established code for axial calculations. We will compare results regarding the ground state and the constrained deformation curves of ^{24}Mg. In section 6.2.2, a more accurate comparison of the deformation curve is presented using the cartesian mesh code `EV8`.

6.2.1. `HFBTHO` code and calculation details

`HFBTHO`

To benchmark the code against a basis expansion method in the case of nuclear deformation, the `HFBTHO` code was used [60], it is a HFB solver which minimizes the energy functional on a (transformed) harmonic oscillator basis. Since ^{24}Mg is a light, bound nu-
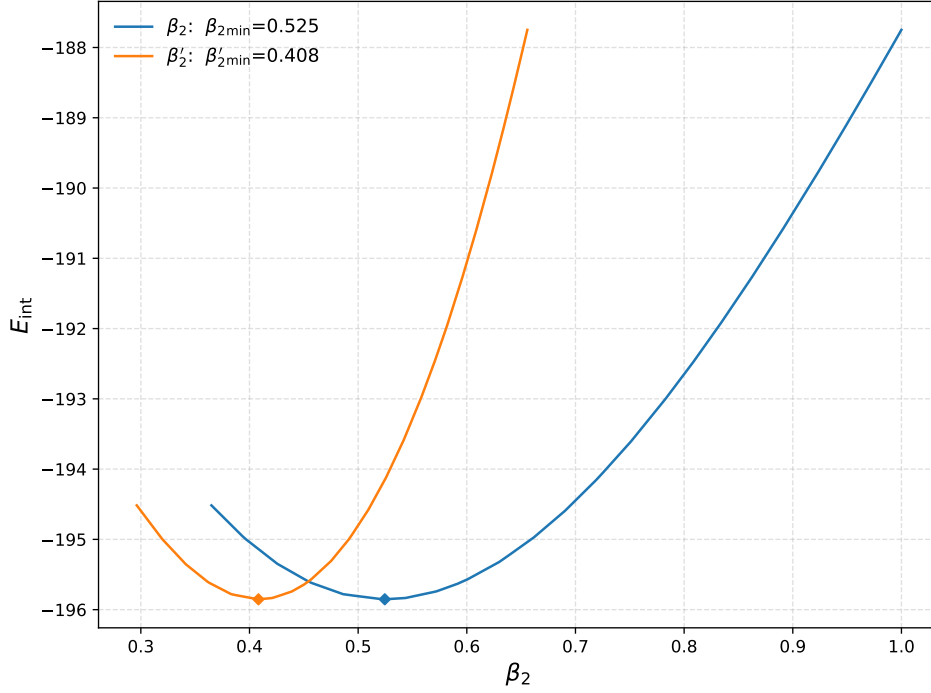
Figure 6.1: Comparison between the two formulae for β_2 in a deformation curve for ^{24}Mg. β_2' refers to the deformation parameter normalised by the parametrised radius, while β_2 refers to the deformation parameter normalised by the actual mean square radius.

cleus, it still works well in this case. All calculations were carried out using 12 oscillator shells and assuming a zero pairing interaction. Default parameters were adopted for the quadrupole constraints. Since the version of HFBTHO used in this work has been compiled with the J^2 terms disabled, we present the results from our code both with and without them. The results obtained without them serve as a benchmark for the code, while those including the J^2 contribution illustrate its impact on the ground state.

Code parameters and axial constraint

As for our code, calculations are performed on a box $[-10, 10]$ fm. In the case of the ground state calculation, a step size of 0.33 fm is used, with a starting guess of a deformed Woods-Saxon with $\beta_2 = 0.4$.

The calculation in the case of the deformation curve is carried out imposing the following constraints

$$\langle \text{Re } \mathcal{Q}_{22} \rangle = \langle \text{Im } \mathcal{Q}_{22} \rangle = 0, \tag{6.6}$$

$$\langle x \rangle = \langle y \rangle = \langle z \rangle = 0, \tag{6.7}$$

$$\langle \mathcal{Q}_{20} \rangle = q_{20}. \tag{6.8}$$

These constraints altogether impose an axial deformation on the system, the constraint on $\langle \mathcal{Q}_{20} \rangle$ alone is not sufficient because on an unconstrained mesh like in our case, the nucleus may deform on a different axis from the chosen one (z) or the $\mathcal{Q}_{20}$ moment may be subject to spurious contributions of a center of mass not centered in the origin; moreover, the axial symmetry of `HFBTHO` doesn't allow broken axial symmetry configurations.

Regarding the stiffness c and damping parameter μ of the ALM described in section 4.3.1, $c = 0.005$ and $\mu = 0.02$ were used. As for convergence criteria, a tolerance of 0.001 on the value of $\beta_2 - \beta_{2,\text{target}}$ was used.

Ground state

Table 6.1 reports data of the comparison for the ground state of ^{24}Mg. In figure 6.2 contours of the density at $y = 0$ are shown, while in figure 6.3 the density viewed 'from the top', ie $z = 0$ is shown. As remarked by the density contours, the ground state is axially symmetric, quadrupole deformed, and parity-defined.

Charge radii for the two codes are displayed but not compared, due to different formulas used for their computation. $\langle x^2 \rangle$, $\langle y^2 \rangle$ and $\langle z^2 \rangle$ are reported for our code but not for `HFBTHO` since it does not compute them.

		GCG	GCG no J^2	`HFBTHO`	Δ	$\Delta\%$
E_{TOT}	[MeV]	-195.854	-197.219	-197.030	0.189	9.52×10^{-2}
$\langle r_n^2 \rangle^{1/2}$	[fm]	3.0124	2.9998	2.9996	0.0002	6.67×10^{-3}
$\langle r_p^2 \rangle^{1/2}$	[fm]	3.0475	3.0346	3.0326	0.0020	6.59×10^{-2}
$\langle r_{ch}^2 \rangle^{1/2}$	[fm]	3.1364	3.1240	3.4614	-	-
$\langle z^2 \rangle^{1/2}$	[fm]	2.145	2.128	-	-	-
$\langle x^2 \rangle^{1/2}$	[fm]	1.511	1.511	-	-	-
$\langle y^2 \rangle^{1/2}$	[fm]	1.514	1.514	-	-	-
β_2	[-]	0.399	0.390	0.390	-	-

Table 6.1: Results for ^{24}Mg ground state, no pairing interaction, box $[-10, 10]$ fm, step size 0.33 fm, SkM* parametrization.

The comparison shows good agreement between the two codes, with the same β_2 minimum and similar ground state properties.
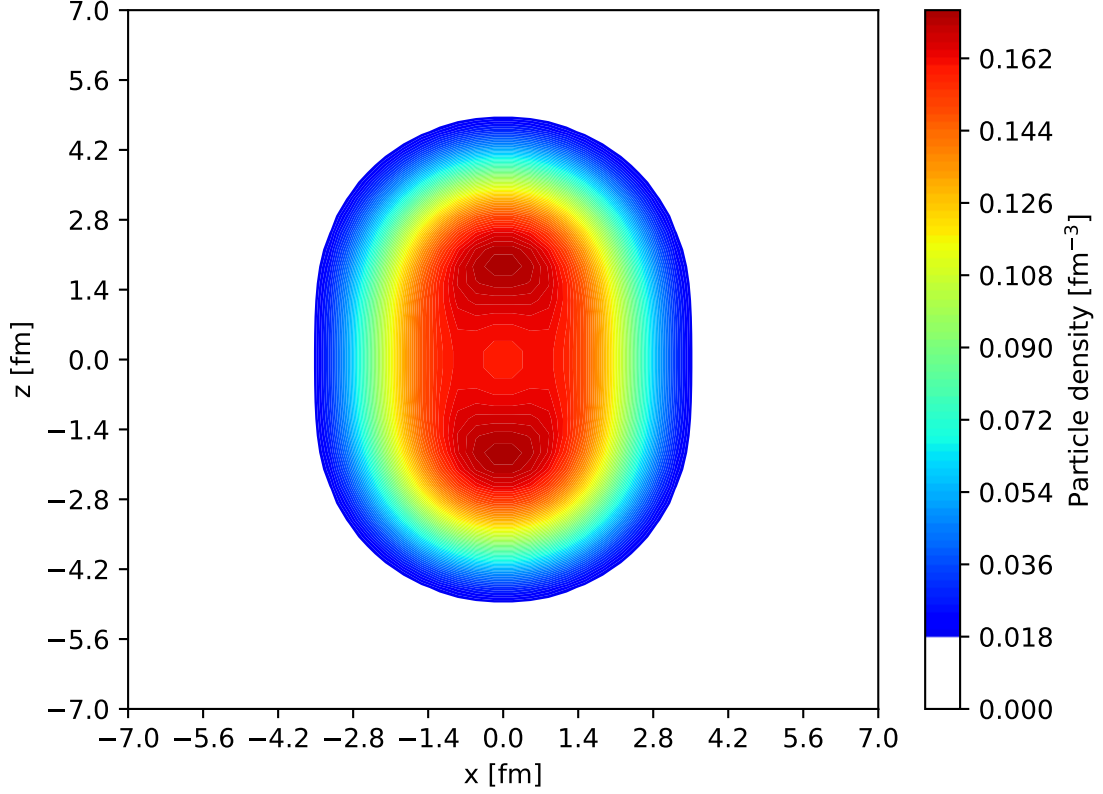
Figure 6.2: ^{24}Mg ground state density $\rho(x, 0, z)$, calculation done on a box $[-10, 10]$ fm, step size 0.33 fm, SkM* parametrization

Deformation curve

In figure 6.4, the deformation curve is shown for ^{24}Mg, without pairing. The quadrupole constraint is imposed for values of β_2 starting from 0.4 fm and going up to 0.65, since the HO expansion stops converging near the requested β_2 after this value, and using a discretisation of 0.02.

Figure 6.4 shows the same trend for both codes, with a minimum of the energy in $\beta_2 = 0.390$, albeit a difference in the energies due to the coarse mesh, a gap which is shown in table 6.1 to shrink when increasing the accuracy of the step size.

6.2.2.   EV8 code and calculation details

HFBTHO can be used to judge how well our implementation fares against other codes for deformed nuclei, but its numerical methodologies are profoundly different from the ones used in our implementation.
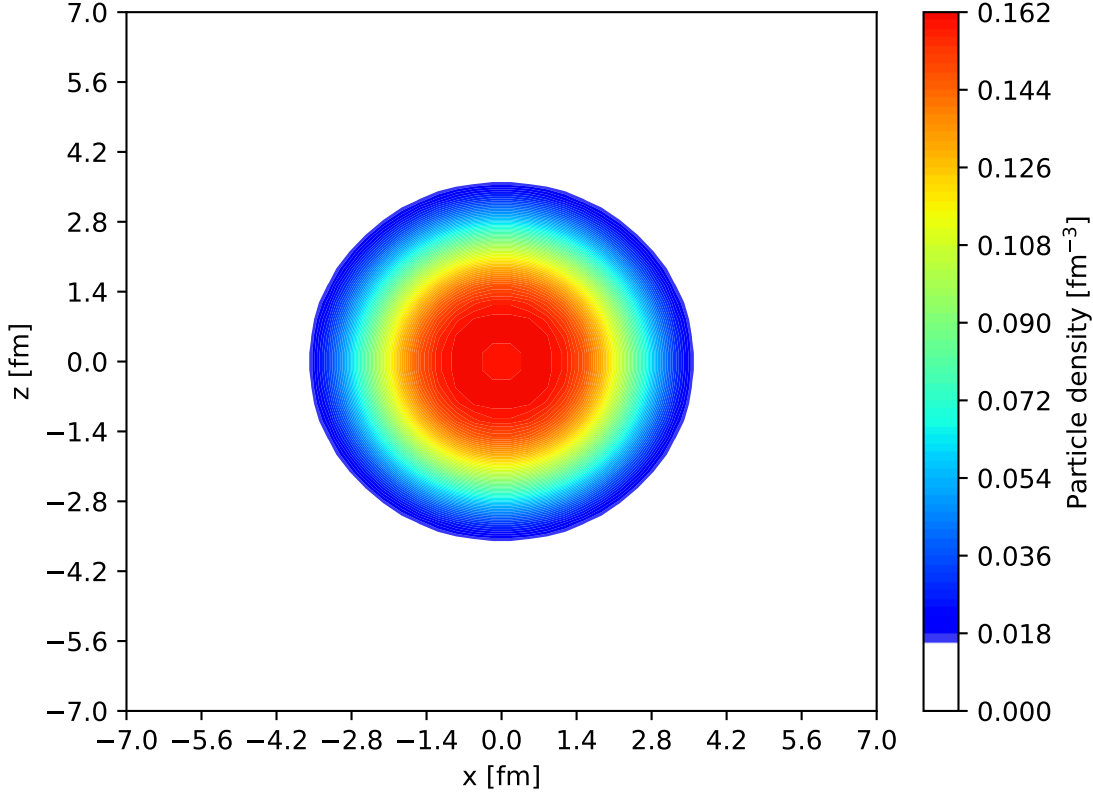
Figure 6.3: ^{24}Mg ground state density $\rho(x, y, 0)$, calculation done on a box $[-10, 10]$ fm, step size 0.33 fm, SkM* parametrization.

An interesting alternative is the `EV8` code [78], which is a HF code that solves the problem on a 3D mesh. Unlike our case, the problem is reduced to a single octant of the box, which allows for quicker computational times, imposing plane reflection symmetry on the three planes $(x, y, 0)$, $(x, 0, z)$, $(0, y, z)$, and the KS equations are discretized using Lagrange derivatives.

EV8 code comparison

Figure 6.5 shows the comparison between the deformation curves of the two codes for ^{24}Mg. The parameters for our calculation are the same as those used in the `HFBTHO` comparison in section 6.2.1, regarding the input parameters of `EV8`, a step size of 0.8 fm, and a number of points on each axis of 32 is used. The results are compared using the definition of β_2 in formula (6.3), which uses a constant radius, hence the apparent wider range of β_2 values compared to the `HFBTHO` comparison in figure 6.4.
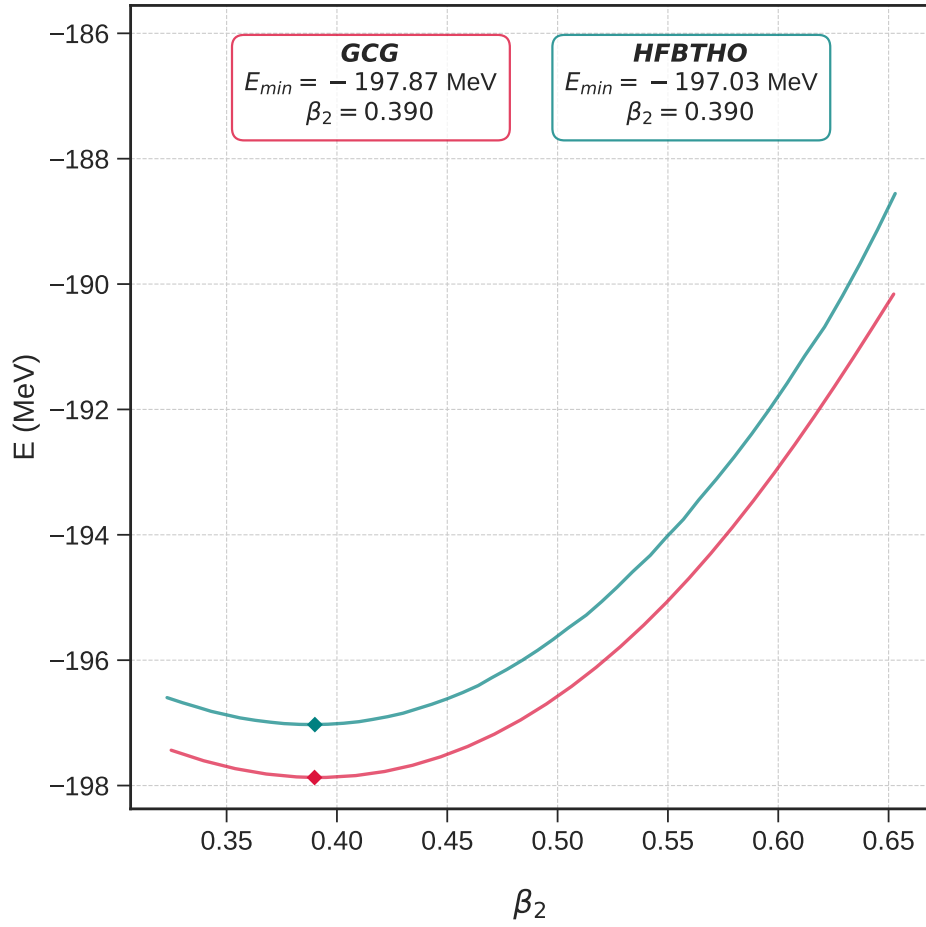
Figure 6.4: ^{24}Mg deformation curve, no pairing interaction, calculation done on a box $[-10, 10]$ fm, step size 0.66 fm, SkM* parametrization, neglecting J^2 terms.

As show by the comparison in figure 6.5, the results are much closer than the ones obtained with the `HFBTHO` code. A slight deviation is still present, likely due to the different numerical methods used by the two codes, both for the KS equations discretization and the minimization of the energy functional.

6.2.3. Deformation curve for different functionals

In figure 6.6, the deformation curves for ^{24}Mg are compared for different Skyrme functionals.
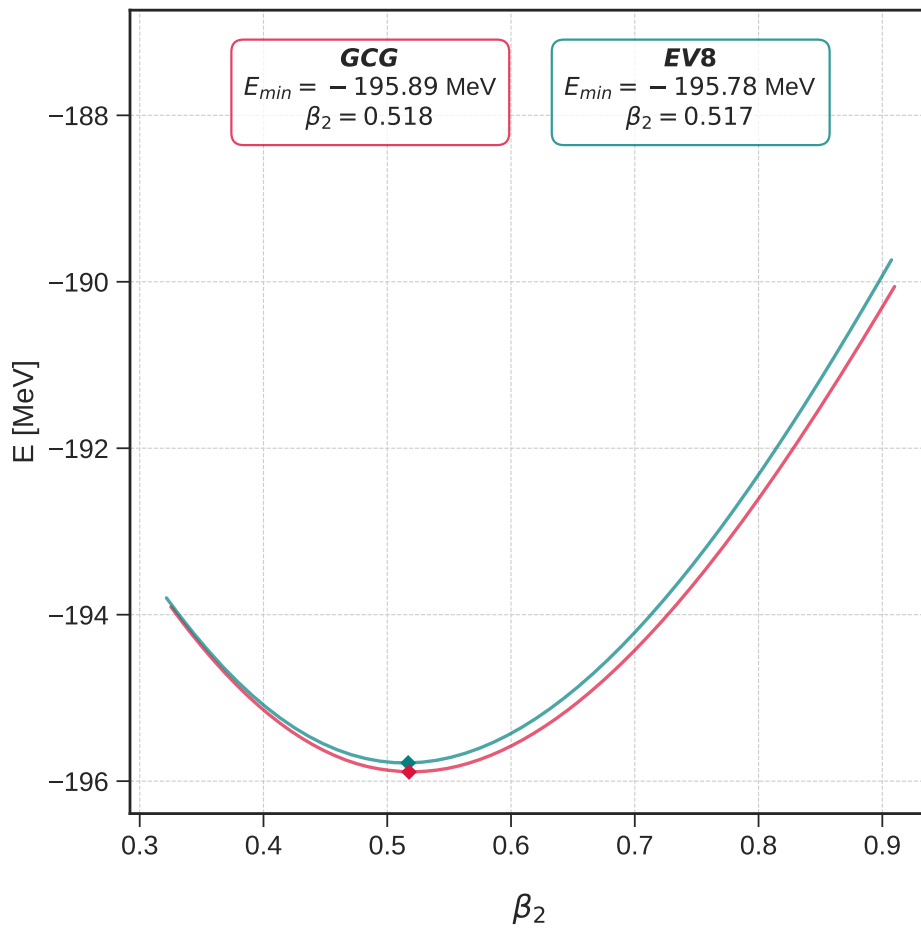
Figure 6.5: Comparison with the `EV8` code for ^{24}Mg, no pairing interaction, box $[-10, 10]$ fm, step size 0.6 fm, SLy4 parametrization.
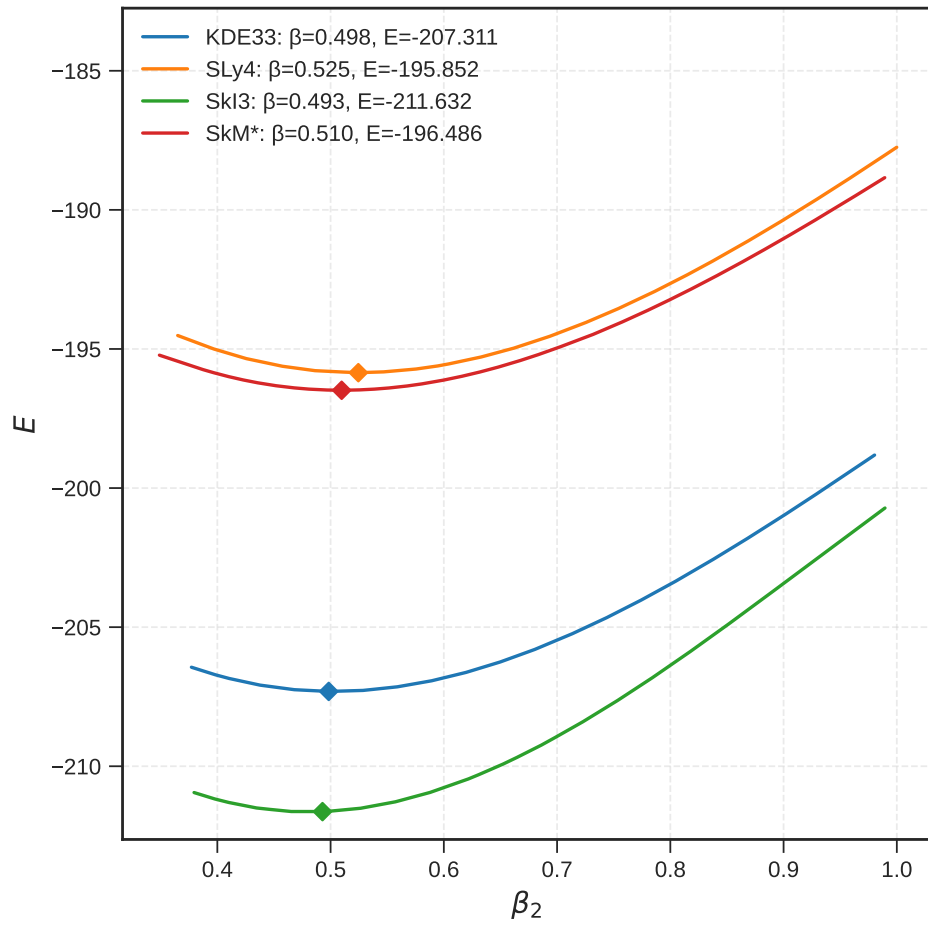
Figure 6.6: Comparison between different Skyrme functionals of the ^{24}Mg deformation curves, box $[-10, 10]$ fm, step size 0.6 fm.

6.3.   Other Results

In this final section, some interesting results that may be obtained only when doing Hartree-Fock on cartesian meshes are presented. In section 6.3.1, some results are presented for the ^{20}Ne nucleus, in particular, the Nucleon Localization Function (NLF) is computed so that the formation of clusters may be studied. In section 6.3.2, the results for two near drip line nuclei are presented, namely ^{42}Si and ^{28}S.

6.3.1. α-clustering in light nuclei

The formation of clusters in light nuclei has been a research focus in recent years [59]. The hypothesis is that some light nuclei tend to form clusters of lighter particles, mainly α-particles, as to minimize their energy, by displaying 'molecular-like' bonds and resonances among the clusters. The formation of such clusters is still unclear, with the following results we show that in the framework presented in this work, the formation of clusters is present in ^{20}Ne.

In the context of many-body calculations, it is very well known that in ab-initio calculations the formation of clusters is strongly observed [33, 48], while their formation when using Skyrme energy functionals is still unclear, some reporting it to be absent [48].

Nucleon localization function

The study of clusters is made possible by the use of the nucleon localization function (NLF) [74], it is a measure of the conditional probability of finding a nucleon in the short vicinity of another one in space. When dealing with spin-saturated nuclei, as is the case of ^{20}Ne, the NLF reduces to

$$C_q(\boldsymbol{r}) = \left[1 + \left(\frac{\tau_q \rho_q - \frac{1}{4}|\nabla \rho_q|^2}{\rho_q \tau_q^{\text{TF}}} \right)^2 \right]^{-1} \tag{6.9}$$

where τ_q^{TF} is the Thomas-Fermi kinetic energy density, defined as

$$\tau_q^{\text{TF}} = \frac{3}{5}(6\pi^2)^{2/3}\rho_q^{5/3}. \tag{6.10}$$

$\alpha-$clustering in ^{20}Ne

In figure 6.7, the total particle densities and proton NLF of ^{20}Ne are shown for different Skyrme functionals. It is possible to observe that while some functionals like KDE33 show

strong peaks in the particle densities, all of the presented functionals display well defined clusters in their respective NLF contours. Note that clustering in the intrisic frame of the nucleus does not necessarily imply clustering in the laboratory frame, for which projection methods are required [34].

6.3.2. Drip line nuclei

The need of a mesh representation to account for weakly bound systems has been greatly remarked in previous chapters (see 1, 2). In this section, results regarding the two near drip line nuclei ^{42}Si and ^{28}S are presented, the former being a neutron-rich nucleus, the latter being a proton-rich nucleus. Being weakly bound systems, taking direct measurements of quantities like radii, deformations through spectroscopy etc, is not possible.

We shall compare the experimental neutron S_n or proton S_p separation energy with the theoretical value calculated using Koopmans' theorem [51]. The theorem states that in a frozen orbitals approximation, where the mean-field is assumed to remain constant after the removal of a particle, the energy required to remove that particle is equal to the eigenvalue of the last occupied single-particle orbital with an inverse sign. This is an approximation to the true separation energy, since it neglects mean-field relaxations and correlation effects. Using Koopmans' theorem is necessary since we have not included the treatment of odd nuclei in the present work, limiting accessibility to only nuclei with even proton and neutron numbers.

^{42}Si

^{42}Si is a deformed, light, neutron-rich nucleus, having $Z = 14$ and $N = 28$, we may look at its ground state neglecting the pairing interaction thanks to the magic number of neutrons, and the closed sub-shell $1d_{5/2}$. In table 6.2, data computed with some functionals is reported, along with the experimental extrapolated binding energy and neutron separation energy. In figure 6.8, the particle density of ^{42}Si is shown for the SLy4 functional.

^{28}S

^{28}S is a deformed, light, proton-rich nucleus, having $Z = 16$ and $N = 12$, we may look at its ground state neglecting the pairing interaction thanks to the closed sub-shell $2s_{1/2}$ and a number of neutrons analogous to the one in ^{24}Mg. In table 6.3, data computed with some functionals is reported, along with the experimental extrapolated binding energy and proton separation energy. In figure 6.9, the particle density of ^{28}S is shown for the SLy4 functional.
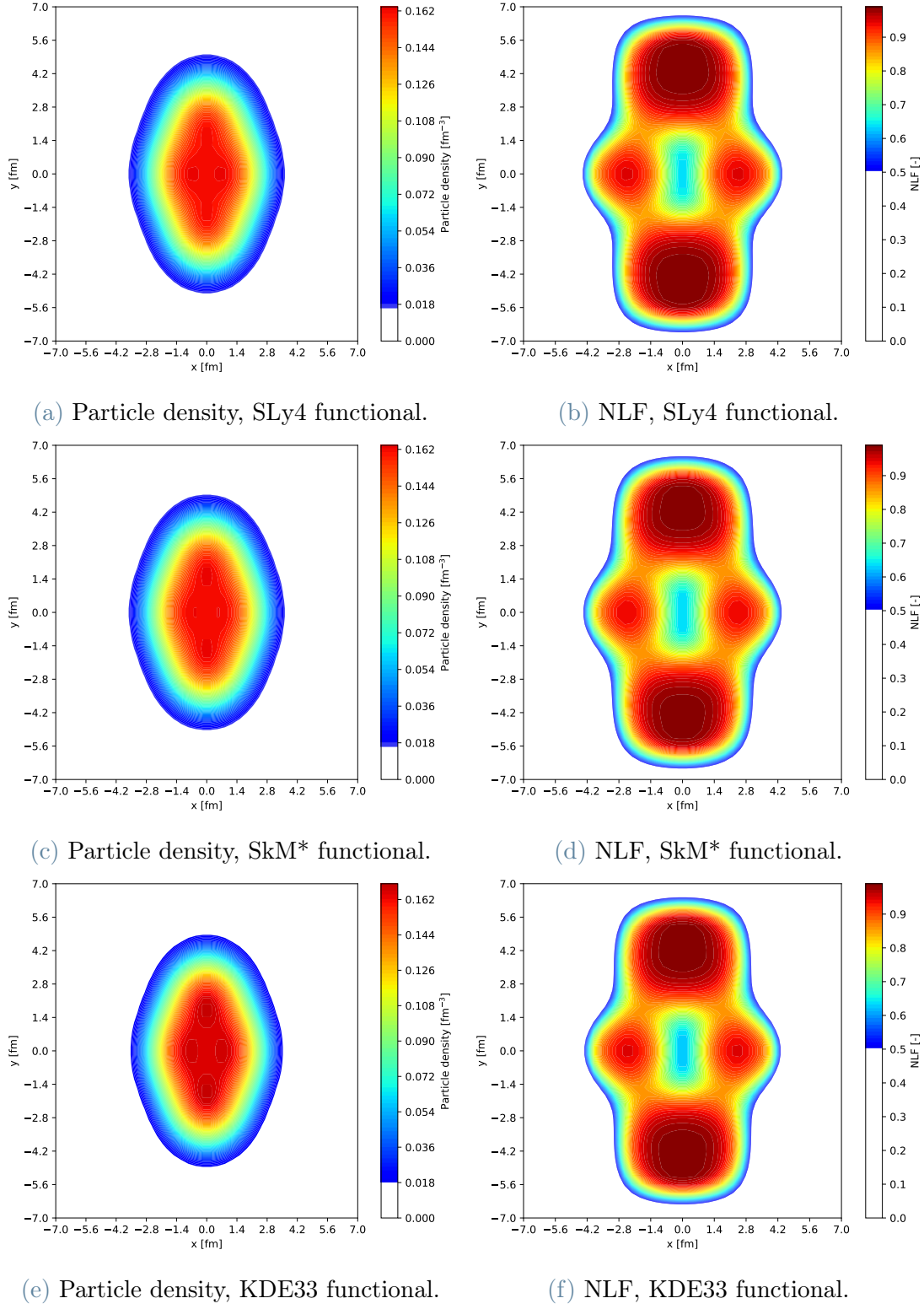
(a) Particle density, SLy4 functional.

(b) NLF, SLy4 functional.

(c) Particle density, SkM* functional.

(d) NLF, SkM* functional.

(e) Particle density, KDE33 functional.

(f) NLF, KDE33 functional.

Figure 6.7: Particle densities and NLFs in ^{20}Ne for different Skyrme functionals.
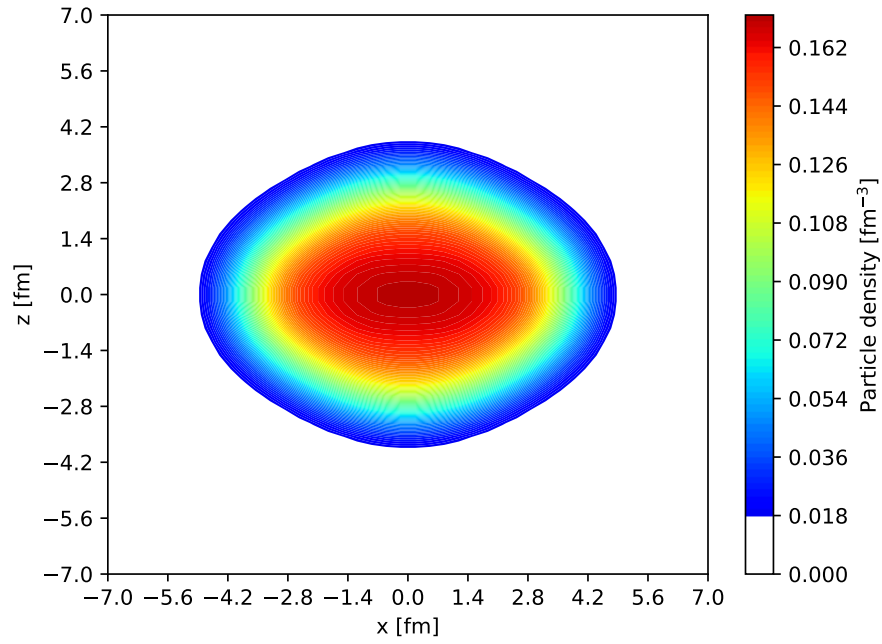
Figure 6.8: ^{42}Si density $\rho(x, 0, z)$, calculation done on a box $[-11, 11]$ fm, step size 0.37 fm, experimental data taken from [1].
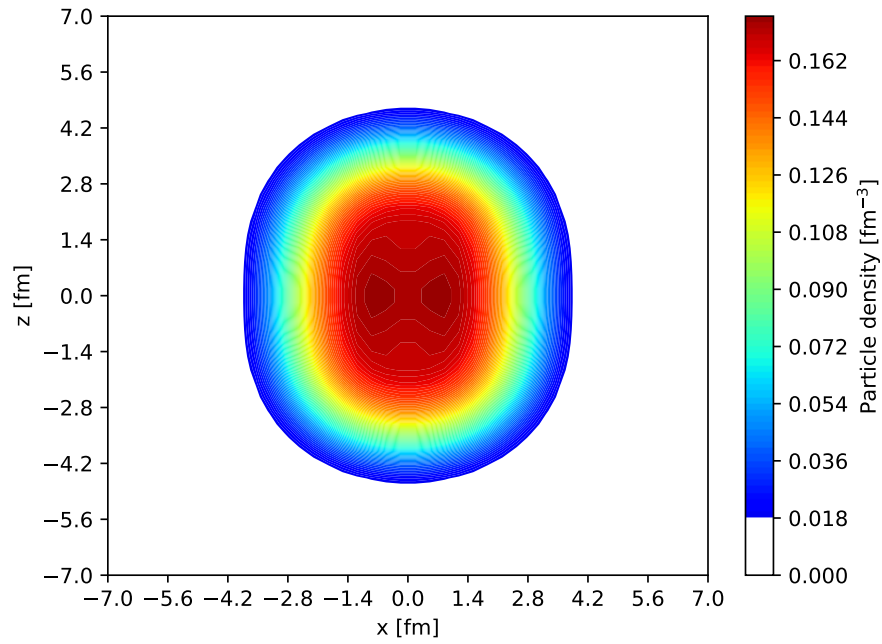

Figure 6.9: ^{28}S density $\rho(x, 0, z)$, calculation done on a box $[-10, 10]$ fm, step size 0.34 fm, experimental data taken from [1].

		SLy4	SkM*	KDE33	SkP	SkI3	Exp.
E	[MeV]	-313.129	-320.760	-326.102	-317.163	-338.047	-311.22
S_n	[MeV]	4.349	4.990	4.132	4.221	5.439	4.458
$\langle r_n^2 \rangle^{1/2}$	[fm]	3.716	3.705	3.666	3.707	3.664	
$\langle r_p^2 \rangle^{1/2}$	[fm]	3.294	3.276	3.247	3.284	3.200	
$\langle r_{ch}^2 \rangle^{1/2}$	[fm]	3.380	3.362	3.334	3.370	3.287	
β_2	[-]	-0.332	0.313	-0.308	-0.302	-0.298	

Table 6.2: Results for ^{42}Si, box $[-11, 11]$ fm, step size 0.37 fm.

		SLy4	SkM*	KDE33	SkI3	Exp.
E	[MeV]	-209.688	-211.642	-221.668	-226.337	-209.406
S_n	[MeV]	3.370	3.330	3.135	3.332	2.556
$\langle r_n^2 \rangle^{1/2}$	[fm]	3.013	2.997	2.964	2.930	
$\langle r_p^2 \rangle^{1/2}$	[fm]	3.235	3.225	3.185	3.168	
$\langle r_{ch}^2 \rangle^{1/2}$	[fm]	3.318	3.308	3.269	3.252	
β_2	[-]	0.314	0.289	0.293	0.315	

Table 6.3: Results for ^{28}S, box $[-10, 10]$ fm, step size 0.34 fm.